Surface Science 714 (2021) 121918

Contents lists available at ScienceDirect

Surface Science

journal homepage: www.elsevier.com/locate/susc

Investigation of (001), (010), and (100) surface termination and surface energies of the Zintl $Ca_5Ga_2Sb_6$ ☆

Monique N. Noel [a,b], David M. Smiadak [b], Jie Pan [b], Yue Qi [b,c], Alexandra Zevalkink [b,*]

[a] Department of Chemistry, Michigan State University, East Lansing, MI 48824, United States
[b] Department of Chemical Engineering and Materials Science, Michigan State University, East Lansing, MI 48824, United States
[c] School of Engineering, Brown University, Providence, RI 02912, United States

ARTICLE INFO

Keywords:
Zintl phase
Surface energy
Surface reconstruction

ABSTRACT

Zintl Phases are a class of intermetallic compounds that combine ionic and covalent bonding to form charge-balanced structures, leading to semiconducting properties. The $Ca_5M_2Sb_6$ family of Zintl compounds, (M =Al, Ga, In), have demonstrated promising thermoelectric efficiency, meaning they can be used to convert a temperature gradient into useful electrical energy. $Ca_5M_2Sb_6$ compounds crystallize in a highly anisotropic structure comprised of chains of corner-linked MSb_4 tetrahedra, in which each neighboring chain is joined via Sb-Sb covalent bonds, forming an infinite polyanionic "ladder". In the present study, we used first principles calculations to study various surface terminations of the $Ca_5Ga_2Sb_6$ structure as a mechanism to understand its crystal growth morphology. Our results indicate that the calcium stoichiometry of the crystal surface plays an important role in surface reconstruction, specifically leading to the formation or breaking of covalent bonds. Our results suggest that surface energy as a function of stoichiometry and crystallographic orientation is only one piece of the puzzle in understanding the growth habits of $Ca_5Ga_2Sb_6$ crystals.

1. Introduction

Pioneered by Zintl [1], Zintl Phases are a class of materials with special interest to solid state chemists and materials scientists, due to their unique bonding and chemistry [2]. Zintl phases are polar intermetallic compounds comprised of highly electropositive cations (typically alkali, alkaline or rare-earth metals) and anions to the right of the so-called Zintl border [3]. In the Zintl-Klemm formalism [4], it is assumed there is a complete transfer of valence electrons from cations to their anionic counterparts. To satisfy the octet rule, the anions follow the 8-N rule for formation of covalent bonds to correct for charge imbalance. The resulting complex structures of Zintls often result in low thermal conductivity and tunable electronic properties—qualities that contribute to their excellent performance as thermoelectric materials [5–8].

One class of Zintl phases, $A_5M_2Sb_6$ compounds (A = Ca, Yb, Sr and M = Al, Ga, and In), [9–13] have been shown to be a promising family of thermoelectric materials and are of interest due to predicted anisotropic transport properties [14,15]. The structure of $Ca_5Ga_2Sb_6$, (orthorhombic, *Pbam*), shown in Fig. 1, is comprised of chains of corner-linked $GaSb_4$ tetrahedra. Each neighboring chain is joined via Sb-Sb covalent bonds to form infinite polyanionic "ladders" aligned in the [001] direction.

The study of anisotropic properties of $A_5M_2Sb_6$ compounds first requires the growth of single crystal samples. Single crystals of Zintl compounds are typically grown using the molten metal flux method [16], which allows for (mostly) unconstrained growth of crystal facets. The resulting crystals are often highly anisotropic in morphology (i.e., plates, needles etc.) which poses an enormous challenge for experimental characterization of transport properties. In addition, the thermodynamic and kinetic factors (e.g., surface energy, bulk diffusion, surface diffusion) controlling the growth habit of Zintl single crystals are not yet well understood. A notable method to investigate underpinnings of crystal morphology utilizes the Wulff relationship [17]. In short, a crystal's shape and exposed surfaces are determined *in part* by the minimized total surface free energy associated with the crystal-medium interface. Those energies, in turn, can also depend on the degree of surface termination and reconstruction (formation of new bonds,

☆ This article is part of the "Young Investigator Special Issue 2021". The CV of the first author can be found under link - https://ars.els-cdn.com/content/image/1-s2.0-S0039602821001229-mmc2.pdf.

* Corresponding author.
E-mail address: alexzev@msu.edu (A. Zevalkink).

https://doi.org/10.1016/j.susc.2021.121918
Received 4 June 2021; Received in revised form 3 August 2021; Accepted 9 August 2021
Available online 18 August 2021

distortion of atomic positions, etc.). Although the importance of Zintls is evident [18], there are very few studies of their surface energies [19], likely due to their complex bonding scheme and large unit cells. In Zintls, any deviation at the surfaces from the bulk stoichiometry is expected to lead to the formation or breaking of covalent bonds, as needed, to preserve overall valence balance.

Our goal in the current study is to draw a connection between surface energy and crystal morphology of the $Ca_5Ga_2Sb_6$ Zintl compound. In this study, we utilize density functional theory (DFT) to investigate the surface energies and surface reconstruction of the (001), (010) and (100) surfaces of $Ca_5Ga_2Sb_6$. Along with various surface planes, we investigate multiple hypothetical surface terminations with varying composition and chemical bonding. These results are compared with the observed morphology of $Ca_5Ga_2Sb_6$ crystals grown from Ga- and Sb- rich molten flux. Ultimately, understanding the mechanisms that govern surface energy of this material may allow for better control of the growth and morphology of Zintl single crystals.

2. Methods

2.1. Synthesis and structural characterization of $Ca_5Ga_2Sb_6$ crystals

Synthesis. High purity elemental Ca (Sigma-Aldrich: dendritic pieces, 99.9%), Ga (Sigma-Aldrich: solid, 99.99%), and Sb (Alfa Aesar: shot, 6 mm & down, 99.999%) were used in the synthesis of polycrystalline $Ca_5Ga_2Sb_6$, which were first ball-milled in five-gram batches using a SPEX MixerMill 8000D for 60 min. Elements were contained inside a stainless-steel jar with two stainless steel balls (dia. = 12.7 mm). Powder samples were then spark plasma sintered in a Dr. Sinter 211LX system under vacuum using 10 mm graphite dies (POCO EDM-3) with graphite foil spacers. Samples were heated to 823 K in five minutes and maintained at that temperature for 10 min to achieve phase-pure polycrystalline $Ca_5Ga_2Sb_6$. The precursor was then mixed with elemental Ga and Sb in an overall molar ratio (73 Ga + 42 Sb + 1 $Ca_5Ga_2Sb_6$) in alumina Canfield crucible sets [20] and sealed within fused silica ampules under vacuum ($< 1 \times 10^{-4}$ torr). These growths were then heated in a box furnace to 1173 K in 12 h, held at temperature for two hours, and slow cooled to 1000 K at a rate of 3 K/h. Ampules were extracted at 1000 K, and centrifuged at 2500 RPM for two minutes [21]. The centrifugation temperature of 1000 K was chosen to be within the $Ca_5Ga_2Sb_6$+ liquid region of the phase diagram. Masses of needle-like $Ca_5Ga_2Sb_6$ crystals with a metallic luster were extracted upon cooling.

Characterization. Scanning electron microscopy (SEM) was conducted on a Tescan Mira 3XMH with samples placed on conducting carbon tape to dissipate residual charge accumulation. Energy-dispersive X-ray spectroscopy (EDX) was performed using an EDAX Apollo X module within the same system with images collected and processed with the TEAM software suite (see Fig. S1). Single crystal X-ray diffraction (SC-XRD) was used to determine the orientation of the crystals (see Fig. S2). SC-XRD was performed using a Bruker-AXS Apex II CCD instrument at 173 K, under a cold nitrogen stream with reflection data acquired using a graphite-monochromated Mo Kα radiation source (λ = 0.71073Å). Data was integrated with SAINT [22]. Single crystals were cut down to an appropriate size with a scalpel. Structures were solved using direct methods and refined on F2 using SHELX [23] subroutines within the Olex2-1.2 crystallographic suite [24]. Reflections were merged using SHELXL with a preliminary rotation image collected to perform the initial quality check and determination of unit cell dimensions.

2.2. Computation methodology

To understand morphology of the $Ca_5Ga_2Sb_6$ crystals, computations were performed to produce surface (slab and vacuum interface) energies of three principal orientations, [001], [010] and [100] of the Zintl antimonide. Slabs were created via the modeling and simulation software program, Materials Studio [25] and structures were analyzed using 3D structural visualization program, VESTA [26]. To investigate interatomic bonding of the slabs, the electron localizability function (ELF) was analyzed [27]. This method provides a more detailed understanding of ionic vs. covalent interactions. The criteria of ELF = 1 corresponds to high electron localization (i.e., a covalent bond or anionic species in ionic bonding) and ELF = 0.5 corresponds to electron-gas-like pair probability (i.e., a metallic bond).

First-principles calculations were performed by the Vienna Ab initio Simulation Package (VASP) [28] based on plane-wave DFT. Core-valence electron interactions were treated using projector augmented wave (PAW) [29] and the semi-local generalized gradient approximation (GGA) of Perdew, Burke, and Emzerhof (PBE) [30] was implemented. The convergence criteria were set to an energy of 10^{-6} eV and force of -0.02 eV/Å for the electronic and ionic steps in relaxation, respectively; surface (100)B used a force of -0.03 eV/Å for convergence. Electronic occupancies were determined using Gaussian smearing and energy width of 0.2 eV in relaxation. The cutoff energy of 400 eV is enough for the convergence of total energy for both bulk and slab structures. The Monkhorst and Pack [31] scheme of 3 × 3 × 5 and 3 × 3 × 1 *k*-point grids was used for the bulk and slab structures, respectively.

The procedure for obtaining the surface energies are described below in (Eqs. (1)–(7)). In general, for a converged stoichiometric slab, the surface energy can be defined as:

$$\gamma = \frac{1}{2A}\left(E_{slab} - NE_{bulk}\right) \quad (1)$$

where A is the area of the surface unit cell, E_{slab} is the total energy of the slab, N is the number of formula units in the surface slab, and E_{bulk} is the energy of one formula unit of corresponding bulk structure. In the present study, the stoichiometry of the slab varies depending on the

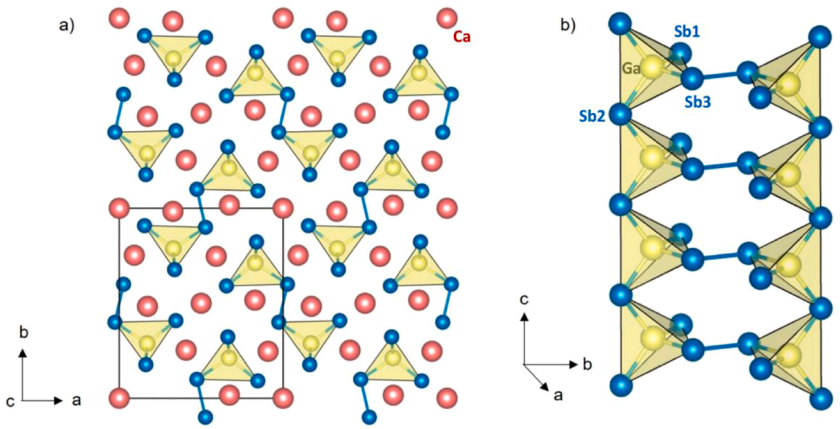

Fig. 1. The $Ca_5Ga_2Sb_6$ structure (**a**) viewed down the c-axis. (**b**) A fragment of one of the polyanionic Ga_2Sb_6 "ladders" which extend infinitely in the c-direction. The needle-shaped $Ca_5Ga_2Sb_6$ crystals grown from flux were oriented along the c-axis. Ca atoms are shown in red, Ga yellow, and Sb blue. **NOTE:** The numbering of Sb atoms is used to identify bond lengths in Table 1. (For interpretation of the references to color in this figure legend, the reader is referred to the web version of this article.).

termination type, thus the Gibbs free energy derived surface equation must include a chemical potential correction. The surface energies of the non-stoichiometric slabs were determined according to:

$$\gamma = \frac{1}{2A}(E_{slab} - NE_{bulk} - \Sigma_i N_i \mu_i) \quad (2)$$

where excess or deficient atoms are accounted for by a chemical potential term for the N_i atoms of species i with chemical potential, μ_i. In our study, we integrate chemical potential corrections in our calculations to accurately predict surface energies of all slab models. This thermodynamic correction is a result of two combined approaches; (1) fitted elemental-phase reference energies (FERE) based on DFT calculations to cancel the errors between the elemental phase and the compound phases, and (2) the change in chemical potential ($\Delta\mu_i$) from elemental to the crystalline Zintl phase represented as:

$$\mu_i = \mu_{iFERE} + \Delta\mu_i \quad (3)$$

Stevandović et al. [32] computed standard earth abundant (transition metals) elemental chemical potentials using the FERE approach (the total energies of pure elemental substances in their conventional reference phase). This approach was calculated to ensure accurate predictions of various compounds thermodynamic stability, with respect to competing decomposition phases, which can be used for predicting the existence and needed growth conditions for new and unknown compounds. The μ_{iFERE} for Ca, Ga, and Sb, respectively are -1.64, -2.37, and -4.29 (eV/atom) [32].

Fig. 2 depicts the computed Ca-Sb-Ga ternary phase diagram as a function of elemental chemical potentials following the procedures outlined in [33]. The phase diagram calculations included multiple binary (e.g., Ca_4Sb_3 & GaSb) and three elemental phases (Ca, Ga, and Sb). At any given point in this map, i.e., a combination of ($\Delta\mu_{Ca}$, $\Delta\mu_{Ga}$, $\Delta\mu_{Sb}$), the thermodynamically stable phases are indicated. The values of chemical potentials can be correlated to synthesis conditions, i.e., the more negative $\Delta\mu_{Ca}$ value, the more the growth environment is Ca-deficient. The black lines are phase boundaries, which are indicative of synthetic conditions at which each complex (phase) can co-exist. The Zintl, $Ca_5Ga_2Sb_6$, is only thermodynamically stable in a very narrow region in the phase diagram, as shown in Fig. 2. Synthesis methodology is in agreeance with the computed diagram. Experimentally, $Ca_5Ga_2Sb_6$ single crystals were precipitated from a Ga- and Sb- rich melt with dilute

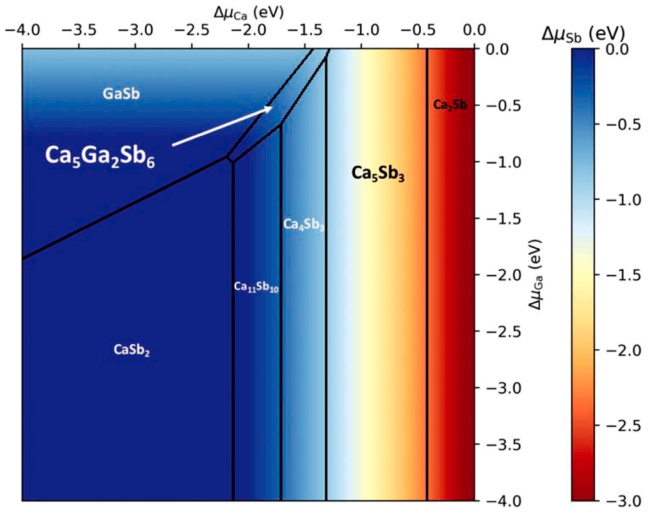

Fig. 2. $Ca_5Ga_2Sb_6$ equilibrium phase diagram. The μ_{Ca} and μ_{Ga} limits are on a 2-D axial plane, while μ_{Sb} is represented by the color scale. $Ca_5Ga_2Sb_6$ is stable in the region indicated by the white arrow. The equilibrium phase boundary line between $Ca_5Ga_2Sb_6$/GaSb established the chemical potential range used in the current study.

Ca, which corresponds to growth conditions near the equilibrium boundary line between the $Ca_5Ga_2Sb_6$ and GaSb phase. Due to the critical interdependence of Ca Ga and Sb chemical potentials, the relationships among $\Delta\mu_i$ are defined as:

$$\Delta H_{GaSb} = \Delta\mu_{Ga} + \Delta\mu_{Sb} \quad (4)$$

$$\Delta H_{Zintl} = 5(\Delta\mu_{Ca}) + 2(\Delta\mu_{Ga}) + 6(\Delta\mu_{Sb}) \quad (5)$$

The DFT computed enthalpy of formation is $\Delta H_{GaSb} = 0.792 \quad eV$ for GaSb and $\Delta H_{Zintl} = -11.88 \quad eV$ for $Ca_5Ga_2Sb_6$. Substituting them into Eqs. (4) and (5) leads to:

$$\Delta\mu_{Ga} = 4.158 + 1.25\Delta\mu_{Ca} \quad (6)$$

$$\Delta\mu_{Sb} = -3.366 - 1.25\Delta\mu_{Ca} \quad (7)$$

Combining both measures, our final surface energy equation can be defined as

$$\gamma = \frac{1}{2A}(E_{slab} - NE_{bulk} - N_{Ca}(\Delta\mu_{Ca} - 1.64) - N_{Ga}(1.25\ \Delta\mu_{Ca} + 1.788) + N_{Sb}(1.25\Delta\mu_{Ca} + 7.656) \quad (8)$$

Due to Ca as the limited reactant, surface energy is plotted as a function of $\Delta\mu_{Ca}$.

3. Results & discussion

3.1. Morphology and orientation of $Ca_5Ga_2Sb_6$ crystals

As shown in Fig. 3a, the morphology of the $Ca_5Ga_2Sb_6$ crystals grown from molten-metal flux can be described as elongated parallelepipeds. In many some cases, multiple crystals appear to be stacked or intergrown. Single-crystal XRD was used to identify the orientation of the $Ca_5Ga_2Sb_6$ crystals (see Fig. 3b), revealing that the longest dimension of the crystals is the [001] direction (which is parallel to the polyanionic "ladders" in the crystal structure) while the (010) family was found to be the most exposed surface. In general, without taking kinetic factors into account, the largest surfaces observed experimentally on the single crystals are expected to be those with the lowest surface energies. Therefore, slab models for the computational study were prepared for (001), (010), and (100) surfaces, and we did not consider any higher-index surfaces here.

3.2. Bulk structure and charge counting

The experimental and computed relaxed lattice parameters of $Ca_5Ga_2Sb_6$, along with selected interatomic distances, are represented in Table 1. The experimental structure was obtained from single crystal X-ray diffraction data and is reported in detail in the supplemental information (see Tables S1 and S2). The present results are consistent with the original structural investigation by Cordier et al. [34]. Electron counting can be used to rationalize the structure of $Ca_5Ga_2Sb_6$ within the Zintl-Klemm formalism: If we assume a formal charge of Ca^{2+} and Ga^{3+}, then a closed shell configuration can only be achieved if two Sb atoms per formula unit form a covalent bond (blue bonds in Fig. 1). This configuration changes the (two) antimony oxidation state from Sb^{3-} to Sb^{2-}, while the remaining four antimony are Sb^{3-}. This leads to an overall valence-precise (balanced) formula of $(Ca^{2+})_5(Ga^{3+})_2(Sb^{2-})_2(Sb^{3-})_4$. Comparing the relaxed computed structure to the experimental structure, we find that the maximum change in bond length is $\leq$ 0.05 Å. The relaxed crystal structure of $Ca_5Ga_2Sb_6$ is shown in Fig. 1. Note that the covalently bonded $(Sb3)^{2-}$ form longer bonds with Ga due to its smaller electrostatic interaction compared with the Ga-$(Sb1)^{3-}$ and Ga-$(Sb2)^{3-}$ bonds.

3.3. Slab Thickness and vacuum gap convergence

A standard practice to calculate surface properties utilizes surface

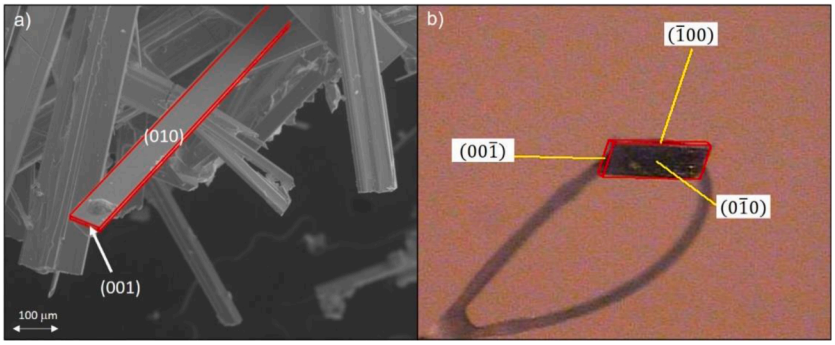

Fig. 3. $Ca_5Ga_2Sb_6$ characterization. (**a**) SEM images of needle-like $Ca_5Ga_2Sb_6$ crystals growing preferentially along the [001] direction. (**b**) single crystal diffraction used to show the most exposed surfaces, the (010) family.

Table 1
Comparison of experimental and computed $Ca_5Ga_2Sb_6$ lattice parameters and bond lengths.

Lattice Parameter (Å)	*Unrelaxed (Experiment)*	*Relaxed (Computation)*
a	12.06	12.13
b	13.98	14.07
c	4.44	4.50
Bond Lengths (Å)		
(2) Ga-Sb2	2.70	2.74
(1)Ga-Sb1	2.68	2.72
(1)Ga-Sb3	2.82	2.85
(1)Sb3-Sb3	2.84	2.89

slabs [35]. Slab (supercell) models, in vacuum, were used to mimic the various surface terminations of $Ca_5Ga_2Sb_6$.Vacuum convergence tests performed using slab [001]A with 10 Å and 12 Å gap yielded a negligible energy difference of only 0.04 eV/atom between the two vacuum sizes. Thereafter, all surface slabs were calculated with a 10 Å vacuum gap to avoid interactions with periodic images. To determine the minimum slab thickness, we applied the Boettger-method [36] to a series of (001)A surfaces. Fig. S3 in the Supplementary depicts absolute convergence (0.68 J/m^2) for a slab with a thickness of 10 Å, equivalent to 4 times the shortest (*c*) direction of the primitive unit cell.

3.4. (001) Surfaces

Before beginning our analysis of surface terminations, we must stress that all the slab models used in this study are charge neutral. It is challenging to assign exact formal charge to the under-coordinated surface ions. Instead, in the following discussions, we will use the same assumptions for the surface Ca and Ga that were used to rationalize the bulk structure in the discussion above. Namely, that the Ca and Ga are fully ionized, giving them a formal charge of 2+ and 3+, respectively. Using this assumption, we can then rationalize the covalent bond breaking and formation between neighboring Sb atoms, within the Zintl-Klemm formalism. In the context of the following discussion, the term "electron deficient" thereby means that there are not enough electrons to allow every Sb to have a filled-octet (e.g., closed-shelled configuration), so that new covalent bonds are needed to satisfy the 8-N rule.

Selection of (001) Surface Terminations. We begin our analysis with the (001) surfaces, which are perpendicular to the polyanionic chains in the $Ca_5Ga_2Sb_6$ structure. Fig. 4 depicts the unrelaxed surface terminations selected for the (001) plane, and the total stoichiometry of each slab is given in Table 2. The surfaces were chosen so as to leave the $GaSb_4$ tetrahedra and the homoatomic Sb-Sb bonds intact. Calcium atoms were then progressively removed in surfaces A-E to allow us to investigate the impact of stoichiometry on surface energy. Emphasis was placed on the calcium surface content, since calcium is the primary electron donor in this system. We project that as the calcium content is

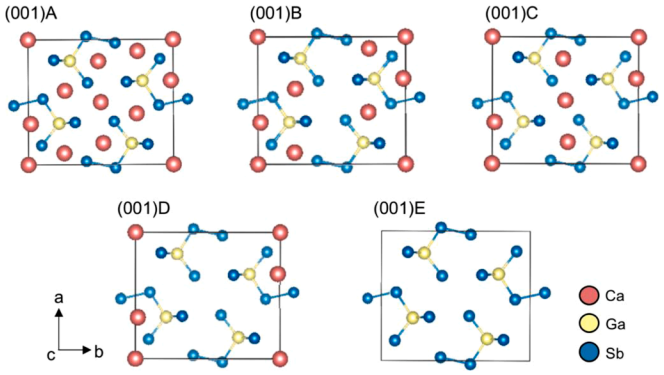

Fig. 4. Unrelaxed (001) surface terminations viewed down the c-axis. The surfaces presented here differ only in the amount of Ca removed from the surface: (001)A-no Ca removed, (001)B-three Ca removed, (001)C-four Ca removed, (001)D-seven Ca removed, and (001)E-all 10 surface Ca atoms removed.

Table 2
Stoichiometry of various (001) surface terminations, listed in order of decreasing Ca content.

Slab name	*Slab stoichiometry*	*Slab stoichiometry emphasizing deviation from bulk $Ca_5Ga_2Sb_6$*
(001)A	$Ca_{50}Ga_{16}Sb_{52}$	$Ca_{10}{\cdot}8(Ca_5Ga_2Sb_6)$ Sb_4
(001)B	$Ca_{44}Ga_{16}Sb_{52}$	$Ca_4{\cdot}8(Ca_5Ga_2Sb_6)$ Sb_4
(001)C	$Ca_{42}Ga_{16}Sb_{52}$	$Ca_2{\cdot}8(Ca_5Ga_2Sb_6)$ Sb_4
(001)D	$Ca_{36}Ga_{16}Sb_{52}$	$Ca_1{\cdot}7(Ca_5Ga_2Sb_6)$ Ga_2Sb_{10}
(001)E	$Ca_{30}Ga_{16}Sb_{52}$	$6(Ca_5Ga_2Sb_6)$ Ga_4Sb_{16}

decreased, new covalent interactions will compensate for the missing valence electrons, thus resulting in surface reconstruction.

(001) Surface Reconstruction. The relaxed (001) surfaces are presented in two figures, together with ELF isosurfaces: the relaxed slabs are viewed along the c-axis in Fig. 5 and down the *c*-axis in Fig. 6. As expected, surface reconstruction is a strong function of calcium content. Take for example slab (001)A, which is Ca-rich relative to the bulk stoichiometry of $Ca_5Ga_2Sb_6$ crystal; Table 2 shows that it has 5 excess Ca^{2+} and 2 excess Sb per surface. If we assign the unbonded Sb a formal charge of Sb^{3-}, we still have an excess of 4 electrons per surface beyond what it is needed for a closed-shell bonding configuration. To balance the charge, four dumbbell-forming near-surface $(Sb3)^{2-}$ atoms can break their covalent bonds to become $(Sb3)^{3-}$. This is borne out by the DFT relaxed surface structure; the Sb-Sb bonds nearest the surface are broken, as evidenced by the increased Sb3-Sb3 distance from 2.89 Å to 3.30 Å in the bulk vs. the relaxed structure, respectively. The ELF isosurfaces for surface (001)A in Fig. 6 exhibit decreased electron

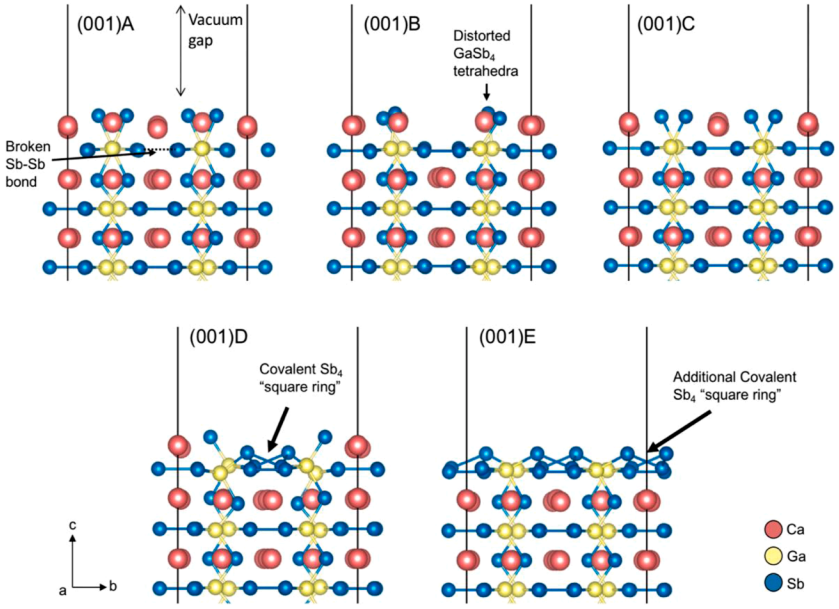

Fig. 5. Relaxed (001) slabs showing varying degrees of surface reconstruction. The progression of covalent bond formation, from slab A to E, suggests the homoatomic Sb-Sb bonds are a direct function of decreasing calcium stoichiometry.

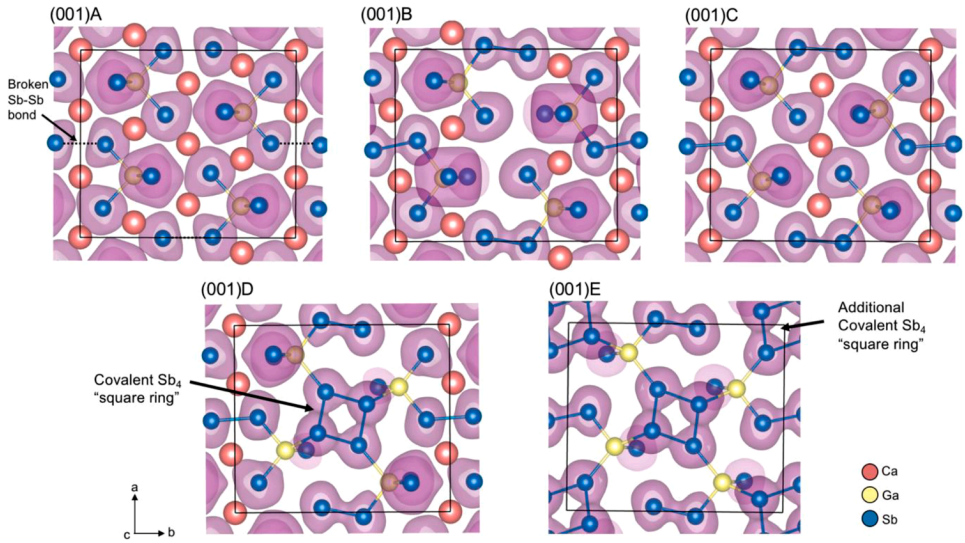

Fig. 6. ELF 3-D isosurfaces for (001) plane surface terminations A-E using a cutoff of ELF=0.6. Slab (001)A depicts breaking of surface Sb-Sb bonds, slabs (001)B and (001)C show only slight changes in atomic coordinates and shift of the Sb lone pairs, while slabs D and E form covalently bonded Sb_4 square rings to make up for the electron deficiency at the surfaces.

localization between the Sb3-Sb3 dumbbells, relative to the bulk, further confirming the broken covalent bonds.

The stoichiometry of slabs (001)B and (001)C are closer to that of the bulk, so we do not observe clear breaking or forming of new Sb-Sb bonds. Slab (001)B has 2 excess Ca^{2+} and 2 excess unbonded Sb per surface. Since each unbonded Sb needs 3 electrons for a filled octet, this equates to a deficiency of 2 e^-/surface. Slab (001)C has 1 excess Ca^{2+} and 2 excess Sb^{3-}, which equates to a deficiency of 4 e^-/surface. Upon relaxation, the Sb in both surfaces shift towards the remaining surface Ca atoms to allow for stronger electrostatic interactions.

Finally, in the most Ca-deficient surfaces, (001)D and (001)E, we observe the formation of Sb_4 "square rings" comprised of Sb1-Sb2 bonds with lengths ranging from 2.93 to 3.07 Å. The Sb atoms in the square rings are each involved in two covalent bonds and can therefore be assigned a charge of 1^-. Without the formation of new covalent bonds, each surface of slab (001)D would have had a deficit of 12 e^-/surface, relative to number needed for each Sb to have a complete valence shell. The formation of one Sb_4 square ring per surface reduces this deficit to only 4 electrons. Likewise, each of the surfaces of slab (001)E would have a deficit of 18 electrons in the absence of reconstruction, but the formation of two Sb_4 square rings on each surface reduces the electron deficit to 2 e^-/surface. In support, new electron localization between the Sb atoms in the square rings confirms the formation of new covalent bonds in surfaces (001)D and (001)E.

3.5. (010) Surfaces

Selection of (010) Surface Terminations. Fig. 7 depicts unrelaxed (top) and relaxed (bottom) surface terminations for the (010) plane; stoichiometries are shown in Table 3. Here again, surface terminations were

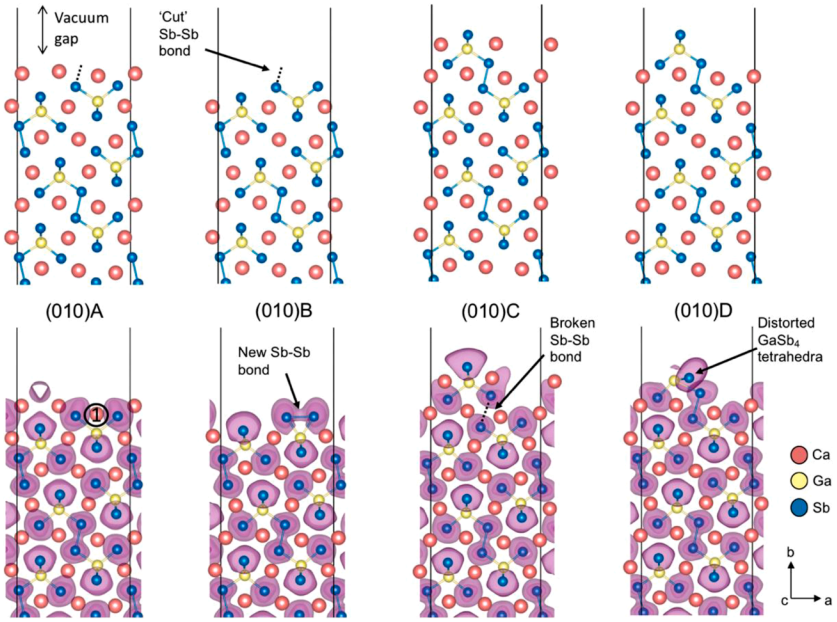

Fig. 7. Unrelaxed (**top**) and relaxed (**bottom**) terminations for selected (010) surfaces. The ELF isosurfaces are shown at a cutoff of 0.6. The unrelaxed cuts presented here differ in the amount of Ca removed from the surface as well as whether the Sb3-Sb3 dumbbell is intact: (010)A)-no Ca removed + cut Sb3-Sb3 bond, (010)B-surface Ca removed + cut Sb3-Sb3 bond, (010)C-no Ca removed + intact Sb3-Sb3 bond, (010)D-surface Ca removed + intact Sb3-Sb3 bond.

Table 3
Stoichiometry of (010) surface terminations. The Sb-Sb dumbbell at the surface of slabs A and B are cut, while surfaces C and D leave the Sb-Sb dumbbell intact.

Slab name	*Slab stoichiometry*	*Slab stoichiometry emphasizing deviation from bulk* $Ca_5Ga_2Sb_6$
(010)A	$Ca_{48}Ga_{18}Sb_{54}$	$Ca_3{\cdot}9(Ca_5Ga_2Sb_6)$
(010)B	$Ca_{42}Ga_{18}Sb_{54}$	$Ca_2{\cdot}8(Ca_5Ga_2Sb_6)\ Ga_2Sb_4$
(010)C	$Ca_{37}Ga_{14}Sb_{42}$	$Ca_2{\cdot}7(Ca_5Ga_2Sb_6)$
(010)D	$Ca_{33}Ga_{14}Sb_{42}$	$Ca_3{\cdot}6(Ca_5Ga_2Sb_6)\ Ga_2Sb_6$

selected such that the $GaSb_4$ tetrahedra remain intact. This orientation affords the opportunity to intentionally 'cut' the homoatomic Sb-Sb bond (as is the case for surfaces (010)A and (010)B).

(010) Surface Reconstruction. As shown in the bottom panels of Fig. 7, reconstruction of the (010) surfaces are highly dependent on the slab stoichiometry. The excess Ca in slab (010)A, relative to the bulk, leads to an excess of 3 e^-/surface. This excess is partly balanced by the intentional cutting of the Sb3-Sb3 bond at the surface, which increases the formal charge of the Sb3 atom at the surface from 2^- to 3^-. We also observe in the relaxed structure a shift in the position of one of the Ca atoms by 0.48 Å along the *b*-direction, toward the nearest $GaSb_4$

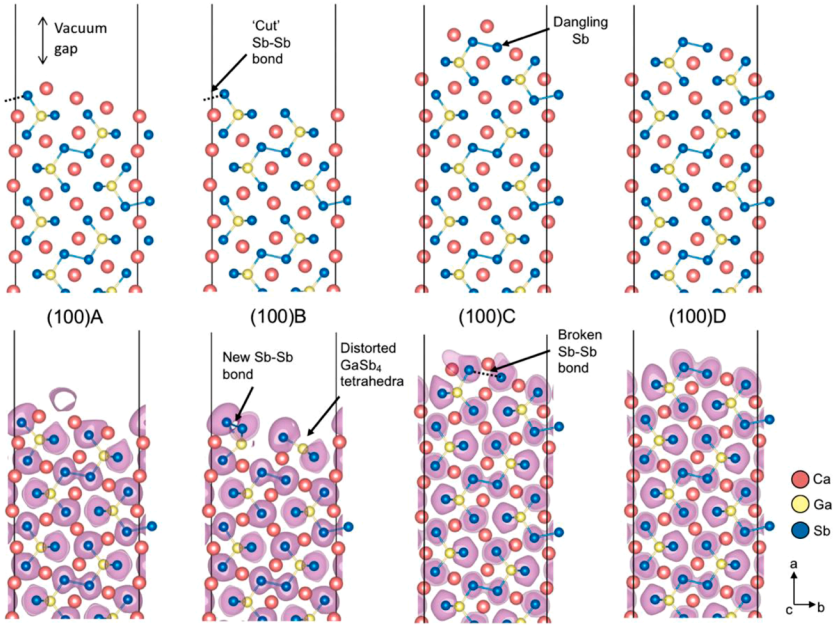

Fig. 8. Unrelaxed (**top**) and relaxed (**bottom**) terminations for selected (100) surfaces. The ELF isosurfaces are shown at a cutoff of 0.6. The initial unrelaxed models here differ in the amount of Ca removed from the surface, as well as keeping the intact $GaSb_4$ tetrahedra-Sb-Sb covalent bond scheme intact: A) no Ca removed + cut dumbbell, B) Ca atoms removed + dumbbell, C) no Ca removed + dumbbell intact, D) Ca atoms removed + dumbbell intact.

tetrahedra (denoted by the number 1 in Fig. 7). Slab (010)B is similar to (010)A, but with all of the surface Ca atoms removed. Accounting for the intentionally broken Sb3-Sb3 bond at the surface, each surface would therefore have an electron deficiency of 1 e^-/surface. The formation of a new Sb3-Sb3 bond (2.93 Å) in the relaxed structure makes up for this imbalance. In surfaces (010)C and (010)D, the Sb3-Sb3 bonds were not intentionally cut. Slab (010)C is Ca-rich relative to bulk $Ca_5Ga_2Sb_6$, with an excess of 2 e^-/surface. As a result, the near surface covalent Sb-Sb bond undergoes breakage, as evidenced by the increase of Sb-Sb distance from 2.89 Å to 3.63 Å in the input & relaxed structures, respectively. Lastly, in slab (010)D, the Ca atoms are removed, leading to an electron deficiency of 2 e^-/surface. Instead of forming new covalent bonds, the surface $GaSb_4$ tetrahedra completely distorts its spatial arrangement to adopt a trigonal planar shape.

3.6. (100) Surfaces

Selection of (100) Surface Terminations. Fig. 8 depicts unrelaxed (top) and relaxed (bottom) surface terminations for the (100) plane; stoichiometries are shown in Table 4. Here again, surface terminations are of varying calcium content. Upon close observation, patterns between (010) and (100) surfaces became apparent. In similar fashion to the (010) series discussed above, (100)A and (100)B are similar, both involving the intentional cutting of one Sb3-Sb3 dumbbell. They are differentiated only by the amount of Ca remaining on the surface. The second set of cuts, (100)C and (100)D, depicts surfaces in which the Sb3-Sb3 dumbbell is left intact, but the topmost $GaSb_4$ tetrahedra missing, leaving a dangling $(Sb3)^{2-}$ at the surface.

(100) Surface Reconstruction. Following similar patterns as the other two principal orientations, reconstruction can be seen in (100) surfaces. Slab (100)A is Ca-rich, leading to an excess of 3 e^-/surface. Similar to the (010)A surfaces, there is no bond-breaking observed in the relaxed surface, formed because the Sb3-Sb3 surface dumbbell was (purposefully) cut in creating the termination. Slab (100)B, in contrast, has a deficit of 4 e^-/surface. This leads to the distortion of the topmost tetrahedron such that a new covalent Sb3-Sb3 bond forms with a length of 2.95 A. Accounting for the new bond gives us a deficit of only 2 e^-/surface. The near-surface tetrahedra also become distorted, forming planar triangular configurations.

In slabs (100)C and (100)D, the Sb3-Sb3 dumbbells at the surface are intact, but the top-most tetrahedra are missing, leaving a dangling $(Sb3)^{2-}$. Thus, for slab (100)C, each surface has 1 excess electron, which leads to the breaking of the Sb3-Sb3 dumbbell. For slab (100)D, each surface has an electron deficiency of 3 e^-/surface. Surprisingly, in this case, no new covalent bonds appear to form near the relaxed surfaces to account for the deficiency. Indeed, the surfaces of slab (100)D show negligible reconstruction upon relaxation. This suggests that 3 e^-/surface may be the lowest charge density the surface can tolerate without Sb-Sb covalent bond forming/breaking.

3.7. Surface energy as a function of $\Delta\mu_{Ca}$

In Fig. 9, we investigated the relationship between surface formation energy and elemental calcium chemical potential, $\Delta\mu_{Ca}$, for all three surface orientations. Chemical potential is a thermodynamic quantity associated with the incremental increase in energy of a system per unit particulate. When two systems are at the same temperature with a single chemical species and the same chemical potential value, there is no net flux of particles from one phase to another. But if the chemical potential differs across the phase boundary, there will be a net flux that is associated with the total energy. Here, this means that increasing $\Delta\mu_{Ca}$ corresponds to a higher concentration of available Ca. The slope of each line is a function of the stoichiometry of the slab. According to Eq. (8), the slope is related to the deviation of the bulk stoichiometry as $-N_{Ca} - 1.25\ N_{Ga} + 1.25\ N_{Sb}$. The N_{Ca}, N_{Ga}, N_{Sb} are listed in Tables 2–4 for each surface termination. In general, Ca-rich slabs have negative slope, becoming more stable with increasing Ca chemical potential, while Ca-poor slabs have positive slope, indicating that the surfaces are more stable in Ca-deficient environments.

The experimental conditions used for crystal growth can be considered to be at the Ca-poor limit, since the crystals grew in a Ga-Sb rich molten metal flux. At the Ca-poor limit of $\Delta\mu_{Ca} = -2.04\ \ eV$ (determined by the phase diagram in Fig. 2) the most stable surfaces for each orientation are (001)B, (010)D, and (100)D. The common characteristic uniting these three lowest-energy surfaces is the absence of significant surface reconstruction. In all three cases, the relaxed surfaces contained the same bonds as the bulk structure and exhibited minimal distortion of atomic positions. A comparison of the surface energies of all three orientations is shown in Fig. 9d. Here, we find that the (001)A and (001)B surfaces have the lowest energy among the investigated surfaces. This result contradicts the observed growth morphology. The single crystals shown in Fig. 3 were found to be highly anisotropic due to more rapid growth in [001] direction than in the [100] or [010] directions, which would indicate that the (001) surface has the lowest surface energy. The disparity between the computed surface energies and the observed crystal habit suggests that kinetic factors (e.g., surface diffusion or diffusion in the liquid flux), in this case, play a more significant role in crystal growth rates than thermodynamic surface energies.

Table 4
Stoichiometry of (100) surface terminations. The Sb3-Sb3 dumbbells at the surface of slabs A and B have been cut, while slabs C and D leave the Sb3-Sb3 dumbbells intact with a dangling Sb3 atom.

Slab name	*Slab stoichiometry*	*Slab stoichiometry emphasizing deviation from bulk $Ca_5Ga_2Sb_6$*
(100)A	$Ca_{43}Ga_{16}Sb_{48}$	$Ca_3{\cdot}8(Ca_5Ga_2Sb_6)$
(100)B	$Ca_{37}Ga_{16}Sb_{48}$	$Ca_2{\cdot}7(Ca_5Ga_2Sb_6)\ Ga_2Sb_6$
(100)C	$Ca_{33}Ga_{12}Sb_{38}$	$Ca_3{\cdot}6(Ca_5Ga_2Sb_6)\ Sb_2$
(100)D	$Ca_{29}Ga_{12}Sb_{38}$	$Ca_4{\cdot}5(Ca_5Ga_2Sb_6)\ Ga_2Sb_8$

4. Conclusion

Surface reconstruction of the (001), (010), and (100) surfaces of the Zintl antimonide, $Ca_5Ga_2Sb_6$ were investigated by analyzing changes in bond lengths and electron localizability in the relaxed DFT structures. Our results show that the degree of surface reconstruction is largely a function of cation:anion ratio, which controls the number of valence electrons available to form covalent bonds in accordance with the Zintl Klemm formalism. Slabs with a high ratio of cations led to the breaking of the Sb-Sb dumbbells, while slabs with a low cation:anion had new covalent bonds form at the surface. We also found that the slabs with the lowest energy overall were those with the least amount of surface reconstruction. Surprisingly, the (001) surfaces were lowest in energy, contradicting expectations based on the observed preferred morphology. Experimental observations showed that the most favorable growth direction was [001] and hence (001) surfaces were expected to have the highest surface energy. We also found only small variation in surface energies amongst all three principal orientations, which again contradicts the observed anisotropic growth. These contradictions lead us to conclude that there are other parameters, most likely kinetic, that affect the growth of $Ca_5Ga_2Sb_6$ crystals in molten flux.

CRediT authorship contribution statement

Monique N. Noel: Investigation, Formal analysis, Writing – original draft. **David M. Smiadak:** Investigation. **Jie Pan:** Investigation. **Yue Qi:** Supervision, Conceptualization, Writing – review & editing. **Alexandra Zevalkink:** Supervision, Funding acquisition, Conceptualization, Writing – review & editing, Visualization.

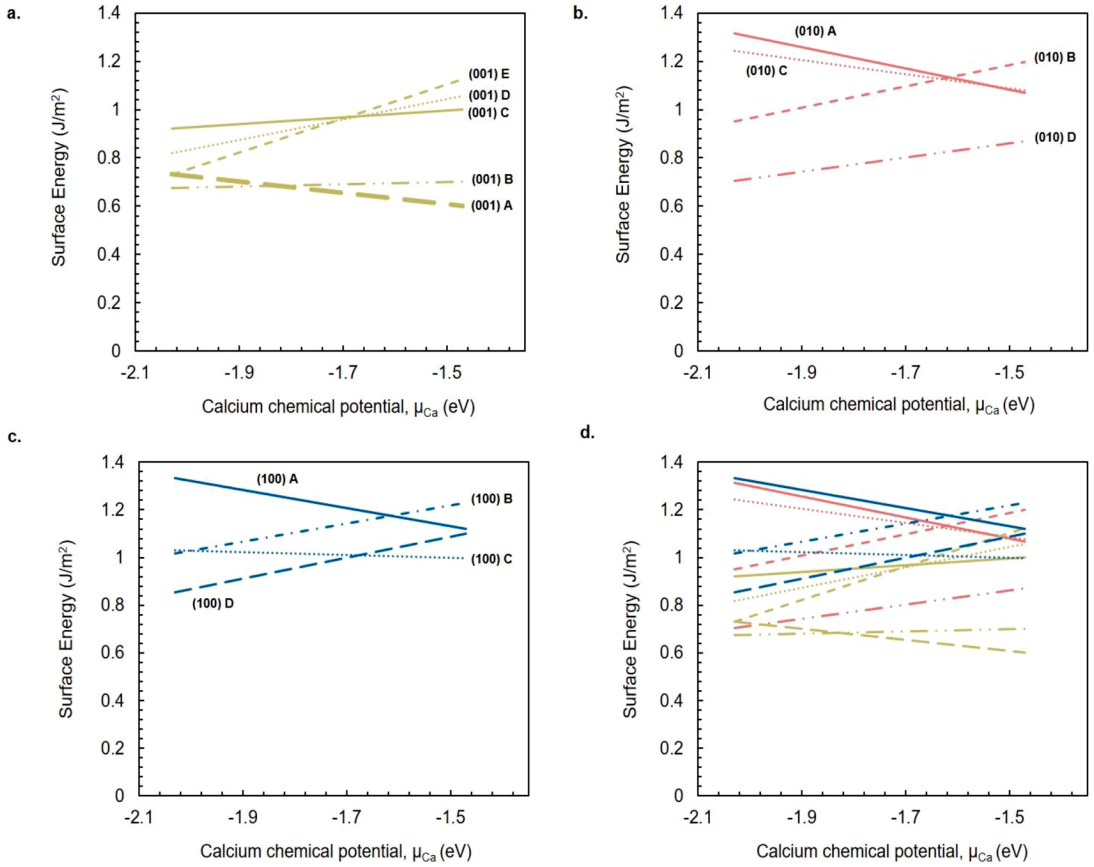

Fig. 9. Surface formation energy, with respect to calcium potential, for all surface terminations. **a.** (001) **b.** (010) **c.** (100) and **d.** overlap of all three orientations. Increasing $\Delta\mu_{Ca}$ corresponds to lower surface energies of Ca-rich surfaces and increases the energy of Ca-deficient surfaces. Overall, (001) series have lower surface energies compared against side planes.

Declaration of Competing Interest

The authors declare that they have no known competing financial interests or personal relationships that could have appeared to influence the work reported in this paper.

Acknowledgments

This work was supported by the National Science Foundation, Graduate Research AGEP Fellowship under contract No. 1709158. The authors gratefully acknowledge Dr. Richard Staples and the Center for Crystallographic Research for help with X-ray crystal analysis. This work was supported in part through computational resources and services provided by the Institute for Cyber-Enabled Research at Michigan State University. We further thank families and friends for their support.

Supplementary materials

Supplementary material associated with this article can be found, in the online version, at doi:10.1016/j.susc.2021.121918.

References

[1] E. Zintl, Intermetallische Verbindungen "intermetallic compounds", Angew. Chem. 52 (1939) 1–6, https://doi.org/10.1002/ange.19390520102.
[2] G.J. Snyder, E.S. Toberer, Complex thermoelectric materials, Nat. Mater. 7 (2008) 105–114, https://doi.org/10.1038/nmat2090.
[3] N. Korber, Metal anions: defining the Zintl border, Z. Anorg. Allg. Chem. 638 (2012) 1057–1060, https://doi.org/10.1002/zaac.201210010.
[4] R. Nesper, The Zintl-Klemm concept - a historical survey, Z. Anorg. Allg. Chem. 640 (2014) 2639–2648, https://doi.org/10.1002/zaac.201400403.
[5] S.M. Kauzlarich, S.R. Brown, G.Jeffrey Snyder, Zintl phases for thermoelectric devices, Dalton Trans. (2007) 2099–2107, https://doi.org/10.1039/B702266B.
[6] E.S. Toberer, A.F. May, G.J. Snyder, Zintl chemistry for designing high efficiency thermoelectric materials, Chem. Mater. 22 (2010) 624–634, https://doi.org/10.1021/cm901956r.
[7] J. Shuai, J. Mao, S. Song, Q. Zhang, G. Chen, Z. Ren, Recent progress and future challenges on thermoelectric Zintl materials, Mater. Today Phys. 1 (2017) 74–95, https://doi.org/10.1016/j.mtphys.2017.06.003.
[8] K.F. Liu, S.Q. Xia, Recent progresses on thermoelectric Zintl phases: structures, materials and optimization, J. Solid State Chem. 270 (2019) 252–264, https://doi.org/10.1016/j.jssc.2018.11.030.
[9] E.S. Toberer, A. Zevalkink, N. Crisosto, G.J. Snyder, The Zintl compound $Ca_5Al_2Sb_6$ for low- cost thermoelectric power generation, Adv. Funct. Mater. 20 (2010) 4375–4380, https://doi.org/10.1002/adfm.201000970.
[10] S.I. Johnson, A. Zevalkink, G.J. Snyder, Improved thermoelectric properties in Zn-doped $Ca_5Ga_2Sb_6$, J. Mater. Chem. A 1 (2013) 4244–4249, https://doi.org/10.1039/c3ta00844d.
[11] A. Zevalkink, J. Swallow, G.J. Snyder, Thermoelectric properties of Zn-doped Ca5In2Sb6, Dalton Trans. 42 (2013) 9713–9719, https://doi.org/10.1039/C3DT50428J.
[12] Y.L. Yan, Y.X. Wang, G.B. Zhang, A key factor improving the thermoelectric properties of Zintl compounds $A_5M_2Pn_6$ (A = Ca, Sr, Ba; *M* = Ga, Al, Pn = As, Sb), Comput. Mater. Sci. 85 (2014) 88–93, https://doi.org/10.1016/j.commatsci.2013.12.049.
[13] U. Aydemir, A. Zevalkink, A. Ormeci, H. Wang, S. Ohno, S. Bux, G.J. Snyder, Thermoelectric properties of the Zintl phases $Yb_5M_2Sb_6$ (*M* = Al, Ga, In), Dalton Trans. 44 (2015) 6767–6774, https://doi.org/10.1039/C4DT03773A.
[14] A. Zevalkink, E.S. Toberer, T. Bleith, E. Flage-Larsen, G.J. Snyder, Improved carrier concentration control in Zn-doped $Ca_5Al_2Sb_6$, J. Appl. Phys. (2011) 110, https://doi.org/10.1063/1.3607976.
[15] A. Zevalkink, G.S. Pomrehn, S. Johnson, J. Swallow, Z.M. Gibbs, G.J. Snyder, Influence of the triel elements (*M* = Al, Ga, In) on the transport properties of $Ca_5M_2Sb_6$ Zintl compounds, Chem. Mater. 24 (2012) 2091–2098, https://doi.org/10.1021/cm300520w.
[16] M.G. Kanatzidis, R. Pöttgen, W. Jeitschko, The metal flux : a preparative tool for the exploration of intermetallic compounds, Angew. Chem. Int. Ed. 44 (2005) 6996–7023, https://doi.org/10.1002/anie.200462170.
[17] G. Wulff, The question of the speed of growth and the dissolution of the *krystall* areas, Z. Kristalogr. 34 (1901) 449, https://doi.org/10.1524/zkri.1901.34.1.449.

[18] S.M. Kauzlarich, Special issue: advances in Zintl phases, Materials 12 (2019) 2554, https://doi.org/10.3390/ma12162554.
[19] L. Schlipf, A. Slepko, A.B. Posadas, H. Seinige, A. Dhamdhere, M. Tsoi, D.J. Smith, A.A. Demkov, Epitaxial Zintl aluminide $SrAl_4$ grown on a $LaAlO_3$ substrate, Phys. Rev. B 88 (2013), 045314, https://doi.org/10.1103/PhysRevB.88.045314.
[20] P.C. Canfield, T. Kong, U.S. Kaluarachchi, N.H. Jo, Use of frit-disc crucibles for routine and exploratory solution growth of single crystalline samples, Philos. Mag. 96 (2016) 84–92, https://doi.org/10.1080/14786435.2015.1122248.
[21] D.M. Smiadak. Single crystal growth and characterization of zintl phase thermoelectric compounds, 2020. defense link: david_smiadak_4_24_20.pdf (msu.edu).
[22] SAINT, Software for Data Extraction and Reduction, Version 6.02, Bruker AXS Inc., Madison, WI, 2002.
[23] G.M. Sheldrick, A short history of SHELX, Acta Cryst. A64 (2008) 112–122, https://doi.org/10.1107/S0108767307043930.
[24] O.V. Dolomanov, L.J. Bourhis, R.J. Gildea, J.A.K. Howard, H. Puschmann, OLEX2: a complete structure solution, refinement and analysis program, J. Appl. Cryst. 42 (2009) 339–341, https://doi.org/10.1107/S0021889808042726.
[25] A. Jain, S.P. Ong, G. Hautier, W. Chen, W.D. Richards, S. Dacek, S. Cholia, D. Gunter, D. Skinner, G. Ceder, K.A. Persson, The materials project: a materials genome approach to accelerating materials innovation, APL Mater. 1 (2013), 011002, https://doi.org/10.1063/1.4812323.
[26] K. Momma, F. Izumi, VESTA 3 for three-dimensional visualization of crystal, volumetric and morphology data, J. Appl. Cryst. 44 (2011) 1272–1276, https://doi.org/10.1107/S0021889811038970.
[27] A.D. Becke, K.E. Edgecombe, A simple measure of electron localization in atomic and molecular systems, J. Chem. Phys. 92 (1990) 5397–5403, https://doi.org/10.1063/1.458517.
[28] G. Kresse, J. Furthmüller, Efficient iterative schemes for *ab initio* total-energy calculations using a plane-wave basis set, Phys. Rev. B 54 (1996) 11169–11186, https://doi.org/10.1103/PhysRevB.54.11169.
[29] G. Kresse, D. Joubert, From ultrasoft pseudopotentials to the projector augmented-wave method, Phys. Rev. B 59 (1999) 1758–1775, https://doi.org/10.1103/PhysRevB.59.1758.
[30] J.P. Perdew, K. Burke, M. Ernzerhof, Generalized gradient approximation made simple, Phys. Rev. Lett. 77 (1996) 3865–3868, https://doi.org/10.1103/PhysRevLett.77.3865.
[31] H.J. Monkhorst, J.D. Pack, Special points for Brillouin-zone integrations, Phys. Rev. B 13 (1976) 5188–5192, https://doi.org/10.1103/PhysRevB.13.5188.
[32] V. Stevanović, S. Lany, X. Zhang, A. Zunger, Correcting density functional theory for accurate predictions of compound enthalpies of formation: fitted elemental-phase reference energies, Phys. Rev. B. 85 (2012), 115104, https://doi.org/10.1103/PhysRevB.85.115104.
[33] J. Pan, J. Cordell, G.J. Tucker, A.C. Tamboli, A. Zakutayev, S. Lany, Interplay between composition, electronic structure, disorder, and doping due to dual sublattice mixing in nonequilibrium synthesis of $ZnSnN_2$:O, Adv. Mater. 31 (2019), 1807406, https://doi.org/10.1002/adma.201807406.
[34] G. Cordier, H. Schäfer, M. Stelter, $Ca_5Ga_2Sb_6$, $Ca_5In_2Sb_6$ and $Sr_5In_2Sb_6$: The first perantimonidogallate and -indates, Z. Naturforsch. B 40 (1985) 5–8, https://doi.org/10.1515/znb-1985-0103.
[35] W. Sun, G. Ceder, Efficient creation and convergence of surface slabs, Surf. Sci. 617 (2013) 53–59, https://doi.org/10.1016/j.susc.2013.05.016.
[36] J.C. Boettger, Nonconvergence of surface energies obtained from thin-film calculations, Phys. Rev. B 49 (1994) 16798–16800, https://doi.org/10.1103/PhysRevB.49.16798.